Cell Reports
Physical Science

CellPress
OPEN ACCESS

Article

Light intensity dependence of the photocurrent in organic photovoltaic devices

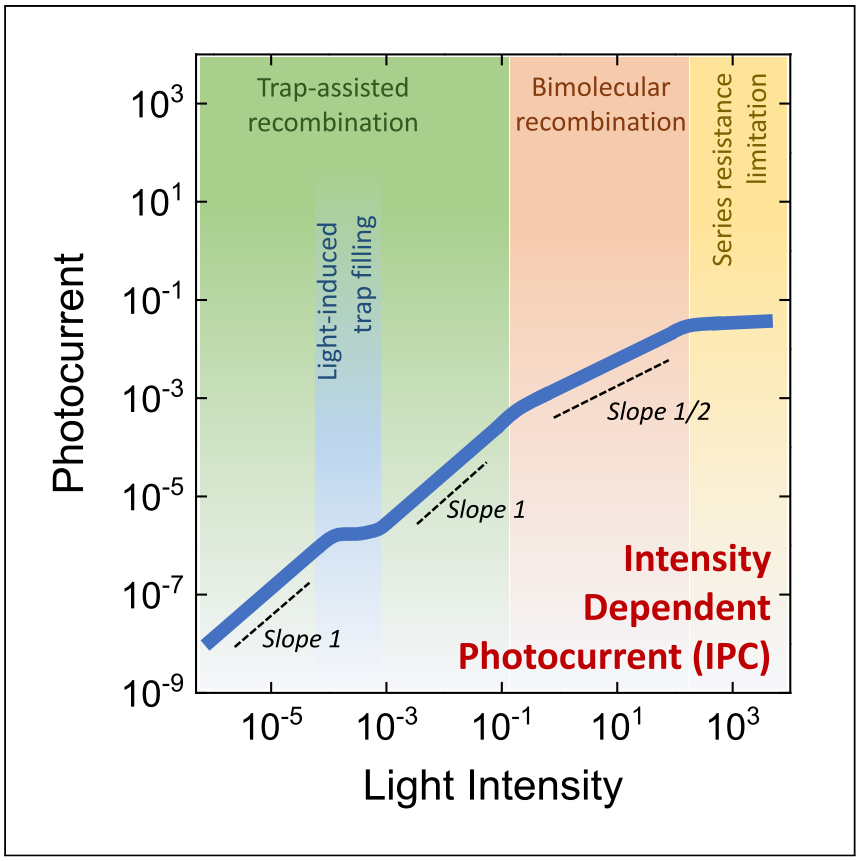

Zeiske et al. present a combined theoretical and experimental study of intensity-dependent photocurrent (IPC), a tool for understanding solar and indoor device fundamentals, to identify different photovoltaic device performance-limiting photocurrent loss mechanisms based on their unique signatures in IPC.

Stefan Zeiske, Wei Li, Paul Meredith, Ardalan Armin, Oskar J. Sandberg

ardalan.armin@swansea.ac.uk (A.A.)
o.j.sandberg@swansea.ac.uk (O.J.S.)

Highlights

IPC is a tool for understanding photovoltaic device fundamentals

Photocurrent loss mechanisms are identified based on their signatures in IPC

The theoretical framework is verified with a drift-diffusion device model

Experimental demonstration of IPC method on state-of-the-art organic solar cells

Zeiske et al., Cell Reports Physical Science 3, 101096
October 19, 2022
https://doi.org/10.1016/j.xcrp.2022.101096

Cell Reports
Physical Science

CellPress
OPEN ACCESS

Article

Light intensity dependence of the photocurrent in organic photovoltaic devices

Stefan Zeiske,[1] Wei Li,[1] Paul Meredith,[1] Ardalan Armin,[1,*] and Oskar J. Sandberg[1,2,*]

SUMMARY

The competition between recombination and extraction of carriers defines the charge collection efficiency and, therefore, the overall performance of organic photovoltaic devices, including solar cells and photodetectors. In this work, we describe different components of the steady-state light intensity-dependent photocurrent (IPC) and charge collection efficiency under operational conditions. Further, we demonstrate how different loss mechanisms can be identified based on their unique signatures in the IPC. In particular, we show how IPC can be used to distinguish first-order, trap-assisted recombination from other first-order photocurrent loss mechanisms, which dominate at the low-intensity characteristic of indoor light-harvesting applications. The theoretical framework is presented and verified by a one-dimensional drift-diffusion device model. Finally, the extended IPC methodology is validated on organic thin-film photovoltaic devices. We conclude that the relatively straightforward measurement of IPC over a large dynamic range can be a powerful tool for understanding solar and indoor device fundamentals.

INTRODUCTION

Photovoltaic devices based on organic semiconductors, including solar cells, indoor photovoltaic cells, and photodetectors, hold great promise for sustainable energy and light-harvesting technologies.[1–4] However, these systems generally suffer from large non-geminate recombination of charge carriers, limiting the collection of photogenerated charge carriers and, ultimately, the performance of organic photovoltaic (OPV) devices and the dynamic range of photodetectors. To improve device performance and overcome this loss mechanism, it is vital to better understand the competition between recombination and extraction of photogenerated charge carriers.[5,6] The effect of non-geminate recombination is strongly dependent on the illumination light intensity. Considering that indoor light photovoltaic cells and photodetectors operate under vastly different light intensity regimes compared with outdoor solar cells, a comprehensive understanding of the intensity dependence of charge collection (over a very broad range of intensities) is needed to chart the full potential of OPV-based technologies.

In general, the light absorption in the active layer (or junction) of an OPV device results in formation of strongly bound electron-hole pairs, so-called excitons.[7–9] Separation of the excitons into free charge carriers is generally a multi-step process. To facilitate this process, an active layer based on a donor (D)-acceptor (A) blend, a bulk heterojunction (BHJ), is typically used. In this structure, excitons generated in D or A phase can diffuse to a D-A interface, undergo charge transfer (CT), and ultimately dissociate into free electrons and holes in the A and D phases, respectively.[7] The

[1]Sustainable Advanced Materials (Sêr-SAM), Department of Physics, Swansea University, Singleton Park, Swansea, Wales SA2 8PP, UK

[2]Lead contact

*Correspondence: ardalan.armin@swansea.ac.uk (A.A.), o.j.sandberg@swansea.ac.uk (O.J.S.)

https://doi.org/10.1016/j.xcrp.2022.101096

electrons and holes are then transported within these phases and extracted at the electrodes. The corresponding photocurrent density J_{ph} at a given excitation wavelength λ and light intensity I_L is given by

$$|J_{ph}| = EQE \times \frac{q\lambda}{hc} I_L, \quad \text{(Equation 1)}$$

where EQE is the photovoltaic external quantum efficiency, h the Planck constant, c the speed of light, and q the elementary charge. The EQE can be further summarized as $EQE = \eta_{abs} \times \eta_{CGY} \times \eta_{col}$, where η_{abs} is the absorptance, η_{CGY} is the quantum efficiency for photogenerated excitons to be converted into free charge carriers, and η_{col} is the charge collection efficiency.

The charge collection efficiency describes the probability that photogenerated charge carriers in the bulk can be extracted at the contacts. Apart from being extracted, on their way to the electrodes, free charge carriers may encounter each other and recombine via a non-geminate process. Because of the low charge carrier mobilities in organic semiconductors, non-geminate recombination is a particularly important loss mechanism in organic solar cells and photodetectors.[6,10] Apart from limiting the short-circuit current density (J_{SC}), recombination is also responsible for loss in the fill factor and open-circuit voltage (V_{OC}), ultimately limiting the power conversion efficiency as well.[6,7,11] In contrast to η_{abs} and η_{CGY}, η_{col} generally depends on I_L. This manifests as a $J_{ph}(I_L) \propto I_L^{\alpha}$ dependence, where $\alpha(I_L)$ is the slope of log J_{ph} versus log I_L and depends on the competition between charge extraction and the dominant charge carrier recombination kinetics within the prevailing intensity regime.[12–15] Importantly, α is not a constant and varies as a function of I_L. Understanding the complex dependence of α on I_L is one of the aims of the work reported here.

The fact that different recombination mechanisms scale differently with I_L and carrier density has been utilized to understand recombination processes in solar cells by using I_L-dependent V_{OC}[16–18] and photocurrent (I_L-dependent photocurrent [IPC]) measurements as well as transient photovoltage (TPV) and charge extraction (CE) techniques.[15,19] However, it has been pointed out that TPV and CE suffer from capacitive effects associated with non-uniform charge carrier distributions, limiting the range of reliable recombination order estimation.[20–22] Intensity-dependent V_{OC} measurements, on the other hand, are very sensitive to parasitic leakage currents at low light intensities and surface recombination of charge carries at the electrodes at high light intensities.[16,23] Finally, IPC measurements offer the possibility to investigate the photocurrent losses as a function of the incident I_L under different operational conditions.[24–28] However, because incomplete dissociation of excitons and intermediary CT states is first order, it has been extremely challenging to distinguish first-order, trap-assisted recombination from the former based on IPC measurements because both scale linearly with carrier density and I_L.

Given this background, it is evident that methods to reliably quantify and distinguish different recombination mechanisms under operational conditions, especially those that are of first order, are currently lacking. In this work, we clarify the influence of different first- and higher-order photocurrent loss mechanisms on the device photocurrent and charge collection efficiency, supported by drift-diffusion simulations. We demonstrate how IPC, when performed sensitively over a broad range of light intensities, can be used to unambiguously differentiate trap-assisted recombination from other first-order losses. This sets IPC apart from other techniques commonly used to study recombination losses in organic solar cells and opens a new window to investigate the photocurrent loss induced by first-order, trap-assisted

recombination. The results are very general and apply to a wide variety of photovoltaic systems, including indoor photovoltaics, concentrator solar cells, and photodetectors.

RESULTS

Theoretical background

We investigate the steady-state photocurrent of a typical OPV diode device based on a BHJ active layer sandwiched between a hole-extracting anode contact and an electron-extracting cathode contact. The analysis is restricted to photocurrents near short-circuit conditions, corresponding to applied voltages V close to zero, where the dark current is negligible. The BHJ active layer is treated as an effective semiconductor where the electron transport takes place in the A, and the hole transport occurs in the D. The anode and cathode contacts are assumed to be situated at $x = 0$ and $x = d$, respectively, where d is the thickness of the active layer.

Under these conditions, the current density is given by the sum of the electron and hole current densities in the active layer, $J_{ph} = J_n(x) + J_p(x)$, where

$$J_n(x) = \mu_n n(x) \frac{\partial E_{Fn}}{\partial x}, \quad \text{(Equation 2a)}$$

$$J_p(x) = \mu_p p(x) \frac{\partial E_{Fp}}{\partial x}. \quad \text{(Equation 2b)}$$

Here, $n(x)$ [$p(x)$] is the density of electrons (holes), E_{Fn} (E_{Fp}) is the quasi-Fermi level for electrons (holes), and μ_n (μ_p) is the electron (hole) mobility. $J_n(x)$ and $J_p(x)$ are also related to the recombination rate $R(x)$ and generation rate $G(x)$ of free charge carriers through the carrier continuity equations

$$G(x) - R(x) + \frac{1}{q}\frac{\partial J_n}{\partial x} = 0, \quad \text{(Equation 3a)}$$

$$G(x) - R(x) - \frac{1}{q}\frac{\partial J_p}{\partial x} = 0. \quad \text{(Equation 3b)}$$

Here, the terms $-\partial J_n/\partial x$ and $\partial J_p/\partial x$ represent the CE rates for electrons and holes (note that $-\partial J_n/\partial x = \partial J_p/\partial x$).

From Equation 1, the charge collection efficiency can then be expressed as

$$\eta_{col} = \frac{|J_{ph}|}{qGd}, \quad \text{(Equation 4)}$$

where

$$G = \frac{\eta_{abs}\eta_{CGY}^{\lambda}}{hcd} I_L \quad \text{(Equation 5)}$$

is the spatial average of the photogeneration rate of free charge carriers in the active layer. For perfect charge collection, $\eta_{col} = 1$, we obtain $|J_{ph}| = qGd$. In this limit, the photocurrent is only limited by first-order losses related to absorption and the charge carrier generation process. In real devices, however, there are likely always charge collection losses induced by recombination. In the general case, η_{col} depends on the charge carrier generation rate, reflected by an intensity dependence of the EQE; this may be expressed as $\eta_{col} \propto I_L^S$, where $S = \alpha - 1$. Only when the photocurrent density is linear with I_L ($\alpha = 1$) will the corresponding η_{col} and, hence, EQE be independent of I_L.

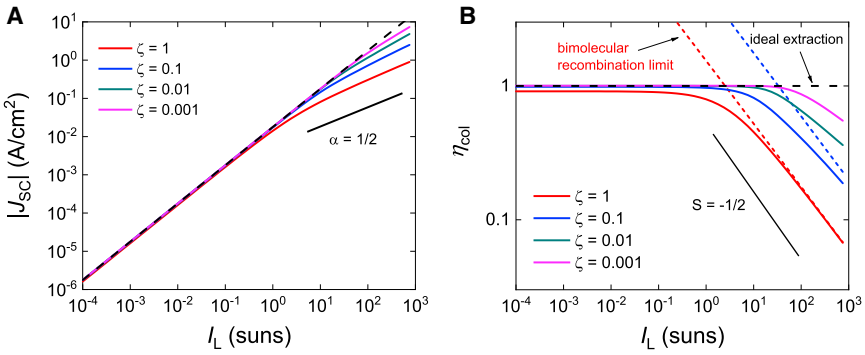

Figure 1. Photocurrent and charge collection under bimolecular recombination

(A) Simulated short-circuit current density (J_{SC}) plotted as a function of light intensity (I_L) and compared for different bimolecular recombination reduction factors between $\zeta = 0.001$ and $\zeta = 1$. The black dashed line represents the case for ideal, loss-free CE.

(B) Same as (A), but instead the charge collection efficiency (η_{col}) is plotted against I_L the light intensity. The analytical expressions of Equation 8 (dotted lines) have been included, assuming balanced mobilities of $\mu_n = \mu_p = 10^{-4}$ cm^2/Vs.

To clarify the effect of recombination on the photocurrent and the charge collection efficiency, we use a one-dimensional drift-diffusion model.[23,29] The device model numerically calculates the current density based on the prevailing charge transport properties, space charge effects, and recombination within the effective semiconductor layer. For the simulations, a device having an active layer thickness of 100 nm with a relative permittivity ε of 3.5 and an electrical D-A energy level gap E_g of 1.3 eV, is considered. We assume selective contacts, $J_n(0) = J_p(d) = 0$, with injection barriers of 0.1 eV for majority carriers. Finally, the charge carrier photogeneration rate is assumed to be uniform throughout the active layer, with an equivalent I_L of 1 sun corresponding to $G = 1.1\times10^{22}$ cm^{-3}s^{-1}.

The competition between CE and bimolecular recombination

We first consider the case of balanced current transport with different degrees of bimolecular recombination in the active layer. This process follows second-order recombination kinetics having a charge carrier recombination rate given by

$$R(x) = \beta n(x)p(x), \qquad \text{(Equation 6)}$$

where β is the bimolecular recombination coefficient. The recombination coefficient is typically expressed relative to the Langevin recombination constant (β_L) as $\beta = \zeta\beta_L$, where ζ is the reduction factor relative to the Langevin rate, and $\beta_L \equiv q(\mu_n + \mu_p)/\varepsilon\varepsilon_0$, where ε_0 is the vacuum permittivity.

Figure 1A shows the simulated (solid lines) J_{SC} as a function of I_L for different recombination constants $\beta = \zeta\beta_L$. The corresponding η_{col} versus intensity is depicted in Figure 1B. The dashed black lines in Figures 1A and 1B represent the limiting cases for perfect charge collection ($\eta_{col} = 1$), with slope parameters of $\alpha = 1$ and $S = 0$, respectively. As shown in Figure 1A (Figure 1B), the photocurrent (charge collection efficiency) is linear (constant) at low intensities, whereas at higher intensities, J_{ph} (η_{col}) starts to deviate from linearity and instead follows a power of 1/2 (−1/2) dependence. The onset of the deviation depends on β and shifts to higher intensity with decreasing ζ.

At high enough photogeneration rates, the bimolecular recombination rate starts dominating over the CE rate in Equation 3. Under these conditions, and

assuming space charge effects to be negligible, Equations 3 and 6 yield $G \approx \beta np$. As a result, J_n and J_p are expected to be equal and uniform throughout the active layer. With the approximation of a constant and equal driving force $\partial E_{Fn}/\partial x = \partial E_{Fp}/\partial x \approx q[V - V_{OC}]/d$ for electrons and holes, it follows from Equation 2 that $\mu_n n = \mu_p p$; hence, $n = \sqrt{\mu_p G/\mu_n \beta}$. Accordingly, the photocurrent $J_{ph} = 2J_n$ is obtained as

$$J_{ph} = q\mu_{eff}\sqrt{\frac{G}{\beta}}\,\frac{(V - V_{OC})}{d} \qquad \text{(Equation 7)}$$

with $\mu_{eff} = 2\sqrt{\mu_n \mu_p}$. Equation 7 represents an upper limit for the photocurrent set by second-order recombination. The associated charge collection efficiency in this limit approaches $\eta_{col} = L_{eff}/d$, where

$$L_{eff} = \frac{\mu_{eff}\tau_\beta[V_{OC} - V]}{d} \qquad \text{(Equation 8)}$$

is an effective charge collection distance that depends on the generation rate via the effective bimolecular recombination lifetime $\tau_\beta = 1/\sqrt{\beta G}$.

As evident from Figure 1, the analytical limits (dotted lines) show good agreement with the numerical drift-diffusion simulations (solid lines) at high photogeneration rates when bimolecular recombination dominates, corresponding to $L_{eff}/d \ll 1$. This also explains the observed slope parameters of $\alpha = 1/2$ and $S = -1/2$, as seen at high light intensities in Figures 1A and 1B, respectively, in accordance with Equation 7.

At low light intensities, when $L_{eff}/d \gg 1$, second-order recombination is negligible, and we expect $J_{SC} \propto G$. Under these conditions, the collection efficiency is constant and close to unity because most of the photogenerated carriers are extracted. The corresponding charge collection loss, resulting in a fixed $\eta_{col} < 1$, can be attributed to effective first-order recombination between injected dark background carriers near the contacts and photogenerated carriers.[30,31] Another source of first-order recombination loss that is present in the case of non-selective contacts is surface recombination; i.e., the extraction of the wrong carrier type at the contacts.[32–36] These first-order losses are generally small at short circuit but may become important for thin active layers and at high injection/voltage levels.

The parameter L_{eff}/d determines the onset of the transition from the linear ($\alpha = 1$) to the nonlinear ($\alpha = 1/2$) photocurrent versus intensity regime, where second-order recombination dominates. The associated onset charge carrier generation rate, corresponding to the generation rate at which $L_{eff}/d = 1$, can be approximated as $G^* = \frac{4\varepsilon\varepsilon_0 V_{oc}^2}{qd^4} \times \frac{\mu_n \mu_p}{[\mu_n + \mu_p]\zeta}$ under short-circuit conditions. Hence, the onset of second-order recombination predominantly depends on the ratio between the smaller charge carrier mobility and the (Langevin) reduction factor ζ.[37] In other words, to avoid significant second-order recombination losses of the photocurrent, the mobilities and ζ must be such that $L_{eff} \gg d$ for a given operating I_L (G).

The effect of an external series resistance

Apart from second-order recombination within the device, the photocurrent at high light intensities will eventually also be limited by the series resistance of the external circuit. For an externally applied voltage V, the actual applied voltage drop across the device is given by $V_{dev} = V - JR_S$, where JR_S represents the resistive voltage

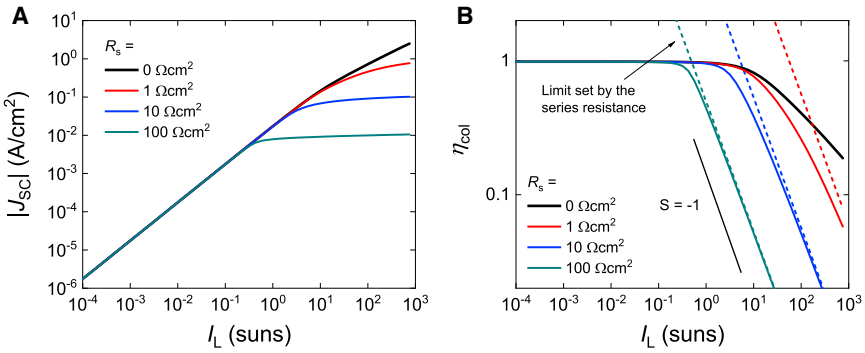

Figure 2. Photocurrent and charge collection in the limit of external R_S

(A) Simulated J_{SC} plotted as a function of I_L, and compared for different series resistances R_S between 0 Ωcm2 and 100 Ωcm^2. At high I_L, the J_{SC} tails off (i.e., $\alpha \rightarrow 0$) to the limit of V_{OC}/R_S set by R_S. (B) Same as (A), but charge collection efficiency (η_{col}) plotted against I_L. Colored dashed lines correspond to the limit set by the R_S estimated in accordance with Equation 10, and the thin, black solid line is a guide to the eye with a slope of $S = -1$ corresponding to theory explained above.

loss across the rest of the circuit (e.g., electrodes, external wires, etc.) having a total specific series resistance R_S in units of Ωcm^2. After accounting for this resistive voltage loss, the high-intensity photocurrent limit in the case of bimolecular recombination (Equation 7) is modified as

$$J_{ph} = q\mu_{eff}\sqrt{\frac{G}{\beta}}\,\frac{(V - V_{OC})}{d}\left[1 + \frac{q\mu_{eff}R_S}{d}\sqrt{\frac{G}{\beta}}\right]^{-1}. \qquad \text{(Equation 9)}$$

Although the effect of the R_S is negligible at small intensities, it becomes prevalent at high intensities because the resistive voltage loss scales with the current.

In the limit of high intensities (large currents), the current density approaches

$$J_{ph} \rightarrow \frac{V - V_{OC}}{R_S}. \qquad \text{(Equation 10)}$$

Equation 10 gives the ultimate upper limit of the photocurrent density as set by the external R_S. This result is independent of the predominant recombination mechanism within the device. In the absence of an external applied voltage (corresponding to a short-circuit condition), the maximum voltage drop across a device under illumination is $V_{dev} = V_{OC}$.

The effect of external series resistive losses is depicted in Figures 2A and 2B, where the I_L-dependent J_{SC} and η_{col}, respectively, are simulated for different R_S. Ideally, the V_{OC} scales as $V_{OC} \propto (kT/q)\ln(I_L)$ with the I_L when bimolecular recombination dominates (kT/q is the thermal voltage). However, in reality, V_{OC} often saturates at high intensity. Ultimately, the short-circuit current tails off under such conditions (i.e., $\alpha \rightarrow 0$), with η_{col} approaching an inverse I_L dependence, manifested by a slope parameter of $S = -1$. The dotted lines in Figure 2B representing the theoretical limits based on Equation 10 are in good agreement with the simulations.

The influence of space charge effects

The above considerations assume nearly balanced electron and hole transport. However, this assumption generally breaks down for conditions when space charge effects dominate inside the active layer. Such conditions may occur when a significant amount of space charge is present in the active layer; e.g., caused by doping or imbalanced mobilities.[12,38–43] A considerable space charge generally induces

an electric field redistribution inside the active layer, resulting in formation of a space charge region (where the electric field is concentrated) and a neutral region (where the electric field is small). Subsequently, the charge collection is efficient only within the space charge region (of width w_{sc}), whereas the collection from the neutral region is limited to a diffusion length L_s from this region.[43] For $w_{sc} + L_s < d$, the photocurrent density can then be approximated as

$$J_{ph} \approx -qG[w_{sc} + L_s]. \quad \text{(Equation 11)}$$

The corresponding charge collection efficiency is given by $\eta_{col} = (w_{sc} + L_s)/d$.

In case of doping-induced space charge, the space charge region is composed of ionized dopants. Under these conditions, w_{sc} and η_{col} are generally expected to be independent of I_L, suggesting $\alpha = 1$. A slight enhancement in η_{col} is expected for low-mobility materials at higher intensities, when the density of photogenerated charge carriers become comparable with the dopant density.[43] The effect of unintentional doping is mainly relevant for thicker active layers (when $d > w_{sc}$) but typically negligible in OPVs with thin active layers.[44]

In the case of imbalanced mobilities, the space charge region is induced by a build-up of photogenerated carriers with the lower mobility at high enough light intensities.[12,45] Specifically, in the case of space charge induced by imbalanced mobilities, it can be shown that $w_{sc} = \sqrt{2\varepsilon\varepsilon_0(V_0 - V)/(qN_{sc})}$ and $L_s = \sqrt{\mu_s kT\tau_\beta/q}$, where μ_s is the mobility of the slower charge carrier.[39] Here, N_{sc} is the mobility-induced space charge density (inside the space charge region) given by $N_{sc} \approx \sqrt{\varepsilon\varepsilon_0 G/(q\mu_s)}$, and V_0 is the built-in potential across the space charge region. Hence, for high enough intensities (and low μ_s) when $w_{sc} \ll d$, the photocurrent is nonlinear and takes the form $J_{ph} \propto G^{3/4}$, following an $\alpha = 3/4$ power dependence of G. If the charge collection from the neutral region is negligible, then the charge collection efficiency simplifies to

$$\eta_{col} \approx \left(\frac{4\mu_s\varepsilon\varepsilon_0}{qG}\right)^{1/4}\frac{\sqrt{V_0 - V}}{d} \quad \text{(Equation 12)}$$

suggesting an $S = -1/4$ power dependence between η_{col} and the I_L.

Figures 3A and 3B show the simulated J_{SC} and the charge collection efficiency plotted as a function of I_L for the case of an increasing mobility imbalance. The mobility ratio varies from balanced mobilities ($\mu_p/\mu_n = 1$) to highly imbalanced mobilities of $\mu_p/\mu_n = 10^{-3}$, assuming $\zeta = \beta/\beta_L = 0.1$ to be fixed in all cases. As shown in Figures 3A and 3B, the onset of the nonlinear regime where $\alpha = 3/4$ depends on the degree of imbalanced mobility (or, rather, the mobility of the slower charge carrier) and shifts to lower intensity the more imbalanced the charge carriers. Dotted lines in Figure 3B are estimated limits in accordance with the analytical expression in Equation 12 for the corresponding mobility ratios. The mobility-induced space charge effect (Equation 12) is competing against the bimolecular recombination-dominated regime (Equation 8) at high intensities because of the strong bimolecular recombination ($\beta/\beta_L = 0.1$). At smaller β/β_L, however, the space charge effect becomes more pronounced (Figure S1).

The effect of trap-assisted recombination

In the case where a significant amount of trap states is present in the bulk of the D-A blend, the recombination of free charge carriers via those sub-gap states becomes dominant at low intensities. This type of non-geminate recombination is referred to as trap-assisted recombination, which is commonly described in terms of

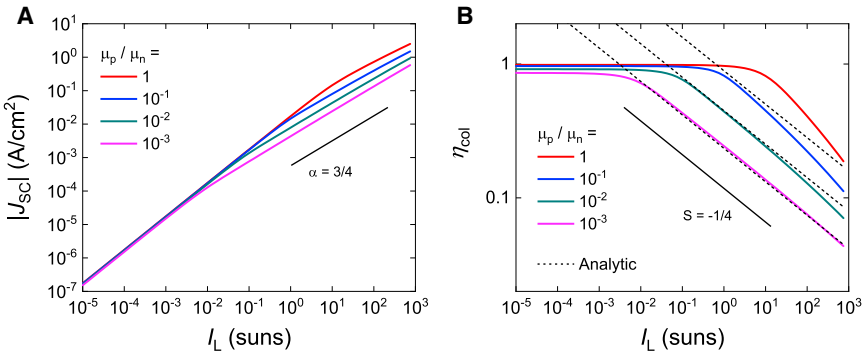

Figure 3. Photocurrent and charge collection under space charge effects

(A) Simulated J_{SC} plotted as a function of I_L and compared for different imbalanced mobility ratios varying between $\mu_n/\mu_p = 1$ and $\mu_n/\mu_p = 10^{-3}$. When the photocurrent density is limited by space charge effects, a slope parameter of $\alpha = 3/4$ is expected in accordance with the above theory.

(B) η_{col} plotted as a function of I_L and simulated for the cases as presented in (A). For comparison, the analytically predicted charge collection efficiencies based on Equation 12 have been included, assuming $\beta = 0.1\beta_L$.

Shockley-Read-Hall (SRH) statistics: a free electron (or hole) is first captured by a trap; the trapped electron (hole) can then recombine with a free hole (or electron). In the case of trap states within the D-A gap, situated at a trap depth Δ_t below the electron transport level, the corresponding trap-assisted recombination rate of free electrons and holes is given by

$$R = \frac{np}{\tau_p(n+n_1)+\tau_n(p+p_1)}, \qquad \text{(Equation 13)}$$

where τ_n and τ_p are the SRH lifetimes for electrons and holes, respectively, and

$$n_1 = N_c \exp\left(-\frac{\Delta_t}{kT}\right), \qquad \text{(Equation 14a)}$$

$$p_1 = N_v \exp\left(\frac{\Delta_t - E_g}{kT}\right). \qquad \text{(Equation 14b)}$$

Here, N_c and N_v denote the effective densities of transport states for electrons in the A and holes in the D, respectively; k is the Boltzmann constant; and T is the temperature.

We first consider the case of mid-gap trap states. In this case, n_1 and p_1 are small. In the low-intensity limit, the carrier densities near the anode and cathode are dominated by dark background holes and electrons, respectively.[35] Thus, we expect $p \gg n$ and, thus, $R = n/\tau_n$, for photogenerated electrons within the hole-dominated (anode-side) region of the active layer. Then, assuming the driving force for CE of photogenerated carriers to be drift-dominated $\partial E_{Fn}/\partial x \approx q[V - V_{bi}]/d$, where V_{bi} is the built-in voltage, Equations 2 and 3 can be readily solved for $J_n(x)$.[46] Concomitantly, we find $J_n(x) = -qGL_n[1 - \exp(-x/L_n)]$, where $L_n = \mu_n\tau_n|V_{bi} - V|/d$ is the electron drift length in the hole-dominated region. A similar treatment can be applied for photogenerated holes within the electron-dominated (cathode-side) region of the active layer, where $n \gg p$ and $R = p/\tau_p$; hence, the hole current density is obtained as $J_p(x) = -qGL_p[1 - \exp([x - d]/L_p)]$, with $L_p = \mu_p\tau_p|V_{bi} - V|/d$ being the hole drift length in the electron-dominated region.

Finally, demanding that $n(d^*)/\tau_n = p(d^*)/\tau_p$, where $x = d^*$ is the point separating the hole- and electron-dominated regions, an approximation for the photocurrent,

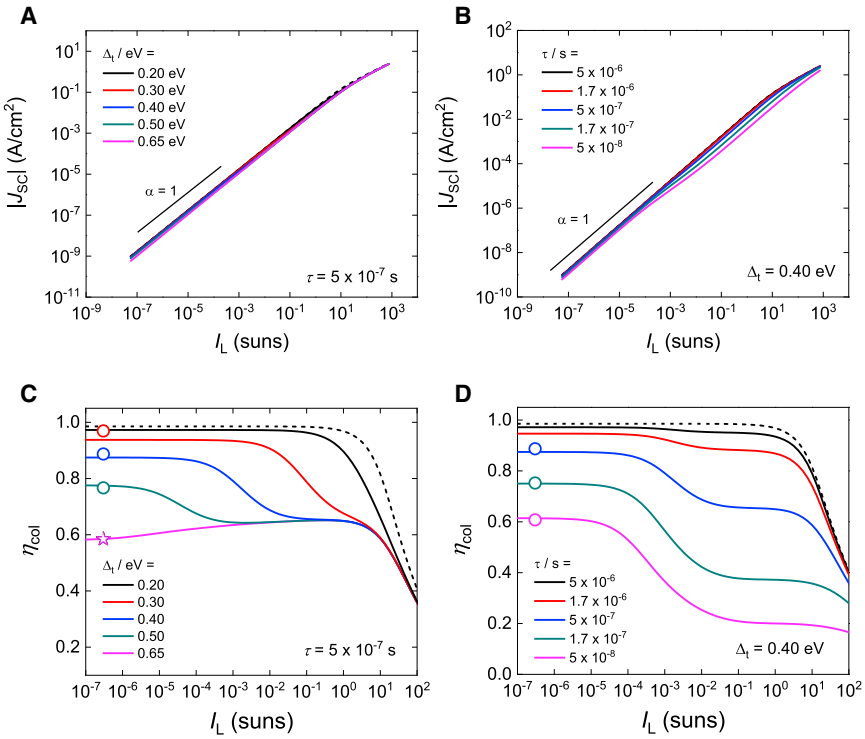

Figure 4. Photocurrent and charge collection in the presence of trap states

(A–D) Simulated J_{SC} (top row) and corresponding η_{col} (bottom row) in the presence of trap states in the D-A bulk for (A and C) varying trap depth Δ_t and constant $\tau_n = \tau_p = 5\times10^{-7}$ s and (B and D) varying SRH lifetimes $\tau_n = \tau_p$ and constant $\Delta_t = 0.4$ eV. Circle (star) symbols correspond to η_{col} determined in accordance with Equation 17 (Equation 15), assuming a built-in voltage of $V_{bi} = 0.84$ V and $b = 0.2$ eV.

$J_{ph} = J_n(d^*) + J_p(d^*)$, can be obtained.[46] Subsequently, when the recombination of charge carriers is dominated by SRH recombination via mid-gap trap states, the corresponding charge collection efficiency at low light intensities is given by

$$\eta_{col} = \frac{L_n + L_p}{d} \times \left[1 - \exp\left(-\frac{d}{L_n + L_p}\right)\right] \qquad \text{(Equation 15)}$$

in accordance with the Hecht equation.[47] Noting that η_{col} is independent of the I_L (i.e., $S = 0$), the photocurrent density is expected to be linear with intensity I_L in this regime; i.e., $\alpha = 1$.

Figures 4A–4D show the simulated J_{SC} and charge collection efficiency as a function of I_L for the case of A-type trap states at varying trap depths Δ_t and SRH lifetimes, assuming $\tau_p = \tau_n$. The photocurrent is indeed found to follow a linear intensity dependence, $J_{SC} \propto G$ ($\alpha = 1$), at low intensities, seen as a constant η_{col} plateau. In the case of mid-gap traps, η_{col} is well approximated by Equation 15 at the lowest intensities (indicated by the star symbol in Figure 4C). However, in the case of shallower trap states, an increased η_{col} is obtained at low intensities (Figure 4), resulting in deviation from Equation 15. This deviation can be attributed to n_1 no longer being negligible in the active layer at low intensities.

The effect of a decreasing Δ_t (i.e., increasing n_1), can be understood by considering photogenerated electrons in the hole-dominated region of the active layer, noting

that the dark hole density is of the form $p(x) \approx N \exp(q[V - V_{bi}]x/[kTd])$,[15] where N is an effective hole density at the anode contact. In the low-intensity limit, the SRH recombination rate via non-mid-gap traps is first order ($R = n/\tau_n$) as long as $p \gg n_1$. However, because of the exponential decay of $p(x)$, at larger distances from the anode, eventually $p \ll n_1$. At these distances, Equation 13 instead simplifies to $R = np/(\tau_n n_1)$, becoming effectively second order, and is thus expected to be negligibly small at low intensities. Assuming $\tau_p \approx \tau_n$ and $p(x_0) = n_1$, the width x_0 of the hole-dominated region, where first-order SRH recombination prevails, can be obtained as

$$x_0 \approx d\frac{[\Delta_t - b]}{q[V_{bi} - V]}. \qquad \text{(Equation 16)}$$

Here, $b = kT \ln(N_c/N)$ represents the energy level bending from accumulated dark holes at the anode contact (assuming $N_v = N_c$). An analogous situation is expected for the electron-dominated region at the cathode.

For non-mid-gap traps, at low intensities, Equation 13 may subsequently be approximated as $R \approx n/\tau_n$ for $0 < x < x_0$ (hole-dominated region) and $R \approx p/\tau_p$ for $d - x_0 < x < d$ (electron-dominated region), whereas $R \approx 0$ otherwise (recombination-free zone). Hence, the charge collection efficiency in the low-intensity limit of a device dominated by SRH recombination via non-mid-gap traps can be approximated as

$$\eta_{col} = 1 - \frac{2x_0}{d} + \frac{L_n\left[1 - \exp\left(-\frac{x_0}{L_n}\right)\right] + L_p\left[1 - \exp\left(-\frac{x_0}{L_p}\right)\right]}{d}, \qquad \text{(Equation 17)}$$

for $x_0 < d/2$. Accordingly, the effect of decreasing the trap depth is to reduce the width x_0 of the hole and electron-dominated regions, resulting in a wider recombination-free zone within the active layer and, thus, an enhanced η_{col}. Indeed, a good agreement between Equation 17 and the simulated η_{col} is seen for non-mid-gap traps at low intensities (indicated by circle-shaped symbols in Figures 4C and 4D).

At higher intensities, however, η_{col} (Figure 4) is seen to undergo a transition into a moderate-intensity regime with η_{col} saturating to an approximately constant value ($\alpha \approx 1$) that is independent of the trap depth. For mid-gap traps, this transition results in a slightly increased η_{col}, whereas for shallower traps, η_{col} is generally decreased relative to the low-intensity limits. This transition can be attributed to the increased density of photogenerated carriers eventually starting to dominate over dark injected carriers inside the active layer. As the photogenerated electron and hole densities become comparable with each other inside the active layer in this case (so that $n \sim p$), Equation 13 instead takes the form $R \sim n/(\tau_p + \tau_n)$. This effectively results in an increased average lifetime for photogenerated charge carriers inside the active layer and, hence, an increased η_{col}.[26,48]

For shallower, non-mid-gap traps, the transition to the moderate intensity regime occurs when the photogenerated carrier density in the active layer exceeds n_1. Under these conditions, a light-induced trap-filling occurs in the bulk (traps start to behave as deep traps), and the trap-assisted recombination in the active layer is no longer negligible, becoming first order ($R \sim n$). This will ultimately result in a reduced charge collection efficiency, appearing as a second η_{col} plateau in the EQE with a lower magnitude (compared with the first one) at moderate intensities. The intensity at which the transition between the low-intensity and the moderate-intensity regime occurs depends on the trap depth, as seen in Figure 4. This unique feature allows SRH

recombination to be distinguished from other first-order losses. It should be noted, however, that SRH recombination between photogenerated charge carriers (at moderate intensities) is also strongly influenced by space charge effects induced by trapped charges.[25]

Finally, we stress that this analysis is limited to SRH recombination via traps within the gap, far away from the conduction and valence level edges. In case of exponentially distributed tail states below the edges,[49,50] however, a different scenario is generally expected. For conditions when trap-assisted recombination via such tail states is the dominant recombination mechanism, it has been suggested that the slope of the photocurrent decreases with I_L, being strongly dependent on the characteristic energy E_U of the trap distribution.[27] However, if space charge from the trapped charge carriers is considerable,[51,52] then we expect the charge collection to be limited by a trap-induced space charge region. This effect is also expected to become more prominent at higher intensities and thicker active layers.[27,51] Under such conditions, the charge collection efficiency is of the form (Note S1; Figure S2)

$$\eta_{\mathrm{col}} \propto G^{-1/(2+2l)} \qquad \text{(Equation 18)}$$

for exponential tail states with $l > 1$, where $l = \frac{E_U}{kT}$. For exponentially distributed tail states, we thus expect S to vary between $S = -1/4$ and $S = 0$ in this case, depending on E_U. The corresponding intensity dependence of the photocurrent is described by $\alpha = 1 - 1/(2+2l)$. This dependence has also been suggested previously by Hartnagel and Kirchartz.[27]

Other recombination orders and effects

The above considerations may be qualitatively extended to the case with a general, but fixed, charge carrier recombination order δ for photogenerated charge carriers. For $p \approx n$, the corresponding recombination rate is of the form

$$R = Bn^{\delta} \qquad \text{(Equation 19)}$$

with the associated recombination coefficient given by B. Provided that $\delta > 1$, and assuming balanced transport ($\mu_n = \mu_p$) and recombination with injected dark carriers to be negligible, the recombination rate term in Equation 3 will be negligible at small intensities (small n) and $J_{\mathrm{ph}} = -qGd$ (i.e., all carriers are extracted). On the other hand, at high intensities, when the recombination term dominates, we have $R \approx G$. In accordance with Equation 3, J_n in this limit is again expected to be uniform in the active layer. Subsequently, from Equation 19, we find $n = (G/B)^{1/\delta}$ and, thus, $J_{\mathrm{ph}} \propto G^{1/\delta}$, corresponding to slopes of $\alpha = 1/\delta$ and $S = (1-\delta)/\delta$. For example, for the case of third-order recombination kinetics ($\delta = 3$), expected in conjunction with Auger recombination, we obtain $\alpha = 1/3$ and $S = -2/3$.

In these analyses we have made several simplifications and assumptions. Most notably, we have assumed effects from the absorption profile and optical interference to be negligible. Such effects generally give rise to non-uniform charge generation profiles within the active layer.[53,54] In thick junctions in particular, where the majority of charge carriers are generated at the transparent contact, space charge effects may become significant.[55] For thin active layers (which is the topic of this work), however, the influence on the photocurrent is expected to remain negligible. At very high light intensities, thermal effects may also start to play a role. These effects are generally associated with a turnover of the V_{OC} with increasing intensity[56] but could also influence the photocurrent. We have also assumed a linear dependence between the carrier generation rate and the I_L (Equation 5), assuming η_{CGY} to be independent of I_L. At very large intensities, however, exciton-exciton annihilation (EEA) may result in a nonlinear dependence between the generation rate and

I_L.[57] Under normal operating intensity conditions, however, these effects are generally negligible in BHJ organic solar cells.

Experimental demonstration

To validate and exemplify the theoretical framework, we next conducted experimental intensity dependent photocurrent (IPC) measurements on OPV cells. The steady-state IPC measurements were performed at an excitation wavelength of 520 nm, and no bias voltage was applied to the devices (short-circuit conditions). From the raw IPC data, we calculated the corresponding EQE versus I_L according to Equation 1. A poly[(2,6-(4,8-bis(5-(2-ethylhexyl-3-fluoro)thiophen-2-yl)-benzo[1,2-b:4,5-b′]dithiophene))-alt-(5,5-(1′,3′-di-2-thienyl-5′,7′-bis(2-ethylhexyl)benzo[1′,2′-c:4′,5′-c′]dithiophene-4,8-dione)] (PM6):3,9-bis(2-methylene-(3-(1,1-dicyanomethylene)-indanone))-5,5,11,11-tetrakis(4-hexylphenyl)-dithieno[2,3-day:2′,3′-d′]-s-indaceno[1,2-b:5,6-b′]dithiophene (ITIC) thin-film BHJ system was selected as a model system to demonstrate the different IPC regimes discussed above. The details of device fabrication are provided in the experimental procedures section. Figures 5A and 5B show the J_{SC} and normalized EQE, respectively, of a 110-nm-thick PM6:ITIC cell measured sensitively over a broad range of light intensities. To demonstrate a device with imbalanced mobilities, IPC was also conducted on a 110-nm-thick poly[(2,6-(4,8-bis(5-(2-ethylhexyl)thiophen-2-yl)-benzo[1,2-b:4,5-b′]dithiophene))-alt-(5,5-(1′,3′-di-2-thienyl-5′,7′-bis(2-ethylhexyl)benzo[1′,2′-*c*:4′,5′-*c*′]dithiophene-4,8-dione)] (PBDB-T):(5Z)-3-ethyl-2-sulfanylidene-5-[[4-[9,9,18,18-tetrakis(2-ethylhexyl)-15-[7-[(Z)-(3-ethyl-4-oxo-2-sulfanylidene-1,3-thiazolidin-5-ylidene)methyl]-2,1,3-benzothiadiazol-4-yl]-5,14-dithiapentacyclo[10.6.0.03,10.04,8.013,17]octadeca-1(12),2,4(8),6,10,13(17),15-heptaen-6-yl]-2,1,3-benzothiadiazol-7-yl]methylidene]-1,3-thiazolidin-4-one (EH-IDTBR) device. A 100-nm-thick PM6:2,2′-((2Z,2′Z)-((12,13-bis(2-ethylhexyl)-3,9-diundecyl-12,13-dihydro-[1,2,5]thiadiazolo[3,4-e]thieno[2″,3″:4′,5′]thieno[2′,3′:4,5]pyrrolo[3,2-g]thieno[2′,3′:4,5]thieno[3,2-b]indole-2,10-diyl)bis(methanylylidene))bis(5,6-difluoro-3-oxo-2,3-dihydro-1H-indene-2,1-diylidene))dimalononitrile (Y6) device was selected as a high-efficiency, state-of-the-art, non-fullerene acceptor organic solar cell; the corresponding short-circuit current densities and normalized EQEs are shown in Figures 5C–5F, respectively. Guided by the theoretical considerations above, different photocurrent loss mechanisms can be identified and will be briefly discussed in what follows.

At low incident light intensities, below equivalent light intensities of $I_L \approx 10^{-4}$ sun, the PM6:ITIC, PBDB-T:EH-IDTBR, and PM6:Y6 devices exhibit a linear photocurrent regime (i.e., $\alpha = 1$, indicated by black solid lines in Figures 5A, 5C, and 5E) that directly translates into constant EQE plateaus (Figures 5B, 5D, and 5F). At moderate intensities, within the range $10^{-3} < I_L < 10^{-1}$ sun, a second linear photocurrent regime can be observed in all three devices. These photocurrent regimes translate into slightly down-shifted, second EQE plateaus indicating the presence of charge carrier recombination via non-mid-gap trap states in the D-A active layer. The corresponding relative loss in the EQE induced by trap-filling in the D-A bulk at moderate intensities amounts to 3%, 5%, and 10% in the PM6:Y6, PBDB-T:EH-IDTBR, and PM6:ITIC devices, respectively (indicated by the gray shaded areas in Figure 5).

At intensities above 1 sun, the photocurrent of the PM6:ITIC device eventually starts to deviate from linearity exhibiting a photocurrent (EQE) versus intensity power dependence of $\alpha = 1/2$ ($S = -1/2$), consistent with bimolecular recombination between free charge carriers dominating over CE in this regime. The corresponding limits set by bimolecular recombination, as expected in accordance with Equation 7, are indicated by the red solid lines in Figures 5A and 5B. The

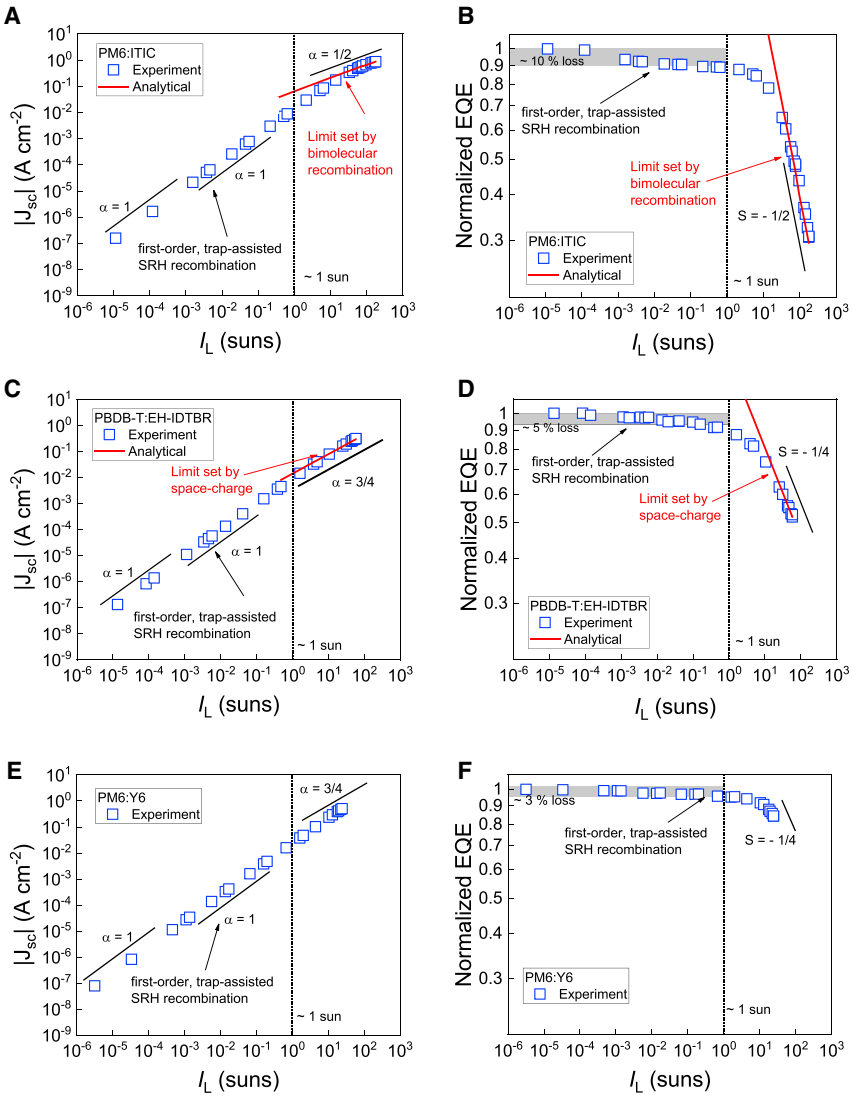

Figure 5. Sensitive, large dynamic range IPC on organic solar cells

(A–F) Experimentally obtained J_{SC} (left column) and normalized EQE (right column) of 110-nm-thick PM6:ITIC (A and B) and PBDB-T:H-IDTBR (C and D), and a 100-nm-thick PM6:Y6 (E and F) OPV cells, measured sensitively over a broad range of intensity. Red solid lines in (A) and (B) represent the limit set by bimolecular recombination calculated in accordance with Equation 7 for $\mu_n \approx \mu_p = 2.0\times10^{-4}$ cm^2/Vs, $d = 110$ nm, and $\beta = 1.6\times10^{-11}$ $cm^{-3}s^{-1}$. The red solid lines in (C) and (D) mark the space-charge-limited photocurrent limit determined in accordance with Equation 12 for $\mu_s = 4.5\times10^{-5}$ cm^2/Vs, $d = 110$ nm, and $\varepsilon = 3.5$. Black solid lines are used as guides to the eye with a slope corresponding to the predominant photocurrent loss mechanism and the theory explained above. Vertical dotted lines marking the 1-sun-equivalent I_L.

estimated limit for the PM6:ITIC is in agreement with the experimental behavior, assuming $\mu_n \approx \mu_p = 10^{-4}$ cm^2/Vs and a bimolecular recombination coefficient of $\beta = 1.6\times10^{-11}$ cm^3s^{-1}.

The PBDB-T:EH-IDTBR device, in turn, suffers at high intensities ($I_L > 1$ sun) from photocurrent losses because of imbalanced carrier mobilities and the build-up of space charge. The red solid lines in Figures 5C and 5D mark the limit set by the imbalanced mobilities estimated in accordance with Equation 12, resulting in a

slower carrier mobility of $\mu_s = 4.5\times10^{-5}$ cm^2/Vs, assuming a dielectric constant of $\varepsilon = 3.5$. This is to be compared with the faster carrier mobility $\mu_f = 6\times10^{-4}$ cm^2/Vs (determined from RPV measurements[25]) suggesting a mobility imbalance of $\mu_f/\mu_s \approx 13$ in PBDB-T:EH-IDTBR.

Similarly, the photocurrent of the PM6:Y6 device was also found to eventually deviate from linearity and seemingly approach a slope of $S = -1/4$ at the highest intensities. This suggests that a build-up of a mobility-induced space charge is dominating at the highest intensities and that β/β_L is small (cf. Figure S1), consistent with the observed mobility imbalance of six and the reduced bimolecular recombination in PM6:Y6.[58] Because of the relatively small mobility imbalance, combined with the reduced bimolecular recombination in this system, mobility-induced space charge effects are expected to remain negligible under 1 sun conditions.[39]

Finally, based on the magnitudes of the EQE plateau at low intensity, referred to as EQE_1, the EQE plateau at moderate intensity, EQE_2, and the transition in between them, one can estimate the trap depth Δ_t for the non-mid-gap trap states, as we have reported in a previous publication.[25] The corresponding Δ_t was estimated to be 0.4, 0.45, and 0.44 eV for the PBDB-T:EH-IDTBR, PM6:ITIC, and PM6:Y6 devices, respectively. Based on these trap depths, we estimate x_0/d of 0.2, 0.25, and 0.24 for the PBDB-T:EH-IDTBR, PM6:ITIC, and PM6:Y6 devices, assuming $V_{bi} = 1$ V and $b = 0.2$ eV. To get a rough estimate of the SRH lifetimes, we assume EQE_1 (EQE_2) to be given by Equation 17 (Equation 15), allowing for a relation between the ratio EQE_1/EQE_2 and L_n/d to be obtained. Here, we assume $L_n \approx L_p$ for PM6:ITIC and $L_n \gg L_p$ for PBDB-T:EH-IDTBR and PM6:Y6, yielding $L_n/d \approx 3.6$, $L_n/d \approx 1.4$ and $L_n/d \approx 1.4$, respectively. Subsequently, with $L_n/d = \mu_n \tau V_{bi}/d^2$, we find an SRH lifetime of $\tau \approx 2.2$ μs for PM6:ITIC, $\tau \approx 0.6$ μs for PM6:Y6, and $\tau \approx 0.3$ μs for PBDB-T:EH-IDTBR.

We expect the influence of EEA and R_S limitations to be negligible in the intensity range chosen to probe the IPC of the three devices. EEA is generally significant at exciton densities above 10^{17} cm^{-3}, whereas for typical exciton lifetimes around 0.5 ns, exciton densities of around 10^{13} cm^{-3} are expected at generation rates equivalent to 1 sun.[57] Hence, EEA is expected to be negligible below intensities corresponding to 1,000 suns. Limitations from the R_S, on the other hand, are negligible as long as the photocurrent is smaller than Equation 10. For our devices, we expect the external R_S to be smaller than 25 Ω. With a pixel area of 0.04 cm^2 of our devices, we then expect resistive effects to be negligible for $J_{SC} < 1.0$ A/cm^2.

DISCUSSION

Based on the above considerations, it is evident that the intensity dependence of the photocurrent and charge collection efficiency can be used as a probe to distinguish between different dominant recombination mechanisms. It is important to note that a simple deviation from linearity (i.e., $\alpha < 1$), does not automatically imply the presence of second-order recombination because nonlinear photocurrent behavior is also obtained for the case of space-charge build-up as a result of imbalanced mobilities or external R_S limitations independent of the underlying dominant recombination mechanism. Table 1 summarizes the expected signatures and expected J_{SC} and EQE power dependences in steady-state IPC measurements for different recombination and photocurrent loss mechanisms. For comparison, the corresponding EQE versus photocurrent power dependence has also been included because this dependence has been frequently reported in the literature.[38,59] Finally, it is important to emphasize that, because the associated photocurrent loss mechanisms

Table 1. Signatures of various photocurrent loss mechanisms in steady-state IPC

	Signature & slope in a log-log plot		
Photocurrent loss mechanism	J_{SC} versus I_L	EQE versus I_L	EQE versus J_{SC}
Ideal (and non-ideal, but constant) charge collection	1	0	0
1st order/monomolecular recombination (absorption and generation loss)	1	0	0
2nd order/bimolecular recombination	1/2	−1/2	−1
1st order, trap-assisted Shockley-Read-Hall (SRH) recombination	two *J*-shifted regimes; 1	two EQE-shifted plateaus; 0	two EQE-shifted plateaus; 0
Imbalanced-mobility-induced space charge	3/4	−1/4	−1/3
Series resistance limitation	$J_{SC} \propto \ln(I_L)$	−1	asymptotically convergent to $J_{SC} \approx V_{OC}/R_S$
Trimolecular Auger recombination	1/3	−2/3	−2

Expected slopes in a log-log plot for relations between short-circuit current density (J_{SC}), external quantum efficiency (EQE), and light intensity (I_L) when different photocurrent loss mechanism are predominant.

vary with intensity, and transition regimes occur in between them, it is important to measure the J_{SC} or, respectively, η_{col} (respectively, EQE) over a broad range of light intensities. Failing to do so may lead to misjudgment of the predominant photocurrent loss mechanisms and the corresponding recombination orders.

To conclude, we have presented a combined theoretical and experimental study aimed at delivering an improved understanding of photocurrent and charge collection efficiency losses and their origins in OPV devices, including solar cells and photodetectors. Our results highlight that different first- and higher-order recombination loss mechanisms show unique intensity dependencies that can be used in IPC measurements when performed sensitively over a broad range of light intensities to unambiguously identify them. In particular, we have shown how IPC, compared with other commonly used measurement techniques, can be used to distinguish first-order, trap-assisted recombination from other first-order photocurrent loss mechanisms.

The results we present here are, in general, not only important for determining predominant recombination loss mechanisms needed to optimize device fabrication and ultimately enhance the efficiency of organic solar cells around 1-sun operational conditions but are also relevant for understanding other light-harvesting devices, such as photodetectors (usually working at low light intensities), indoor photovoltaic applications (working regime of $\sim$ 1/100 sun intensities) and concentrator solar cells (performing under multiple sun intensities[60]).

EXPERIMENTAL PROCEDURES

Resource availability

Lead contact

Further information and requests for resources and materials should be directed to, and will be fulfilled by, the lead contact, OJS (o.j.sandberg@swansea.ac.uk).

Materials availability

This study did not generate new unique materials.

Data and code availability

The data that support the findings of this study are available from the corresponding authors upon reasonable request.

Steady-state intensity-dependent photocurrent measurements

A commercial laser with variable output power was used as a light source and modulated at a low frequency (<0.1 Hz) using a function generator (Keysight Technology, 33500B series). The light perturbation allowed precise and noise-reduced measurements of the external photocurrent. Here, the choice of modulation frequency f was limited by the technical aspects of the IPC setup itself and the physical processes governing the device under test (DUT) (e.g., charge carrier transport, [de]trapping time, and RC time of the circuit). A motorized two-wheel attenuator (Standa, 10MCWA168) containing different optical density (OD) filters was used to vary the input light intensity. The combination of variable laser output power and two-wheel attenuator with a low-frequency photocurrent modulation allowed sensitive measurements of the photocurrent over I_L of multiple orders of magnitude. A silicon (Si) reference photodiode (Thorlabs, SM05PD1A) was used for light power calibration and *in situ* intensity tracking. Two source-measure units (Keithley 2450) were used to simultaneously read the DUT photocurrent and Si photodiode current, while different bias voltages could be applied on the DUT. For the initial calibration process, an additional NIST-calibrated silicon photodiode power sensor (Thorlabs, S121C) was used.

Device fabrication

The PBDB-T:EH-IDTBR (PM6:ITIC and PM6:Y6) solar cell was fabricated with inverted (conventional) device architecture: glass/ITO/ZnO/active layer/MoO_3/Ag (glass/ITO/poly(3,4-ethylenedioxythiophene) polystyrene sulfonate (PEDOT:PSS)/active layer/2,9-bis[3-(dimethyloxidoamino)propyl]anthra[2,1,9-def:6,5,10-*d′e′f′*]diisoquinoline-1,3,8,10(2*H*,9*H*)-tetrone (PDINO)/Ag). Detergent solution was used to clean the commercial ITO patterned glass electrodes for 10 min, followed by a series of ultra-sonication in distilled water, acetone, and 2-propanol, each for 10 min. Prior to oxygen plasma treatment, a nitrogen stream was used to dry the substrates. The ZnO electron transport layer was prepared by dissolving 200 mg zinc acetate dihydrate (Sigma-Aldrich) in 2 mL 2-methoxyethanol (Sigma-Aldrich) using 56 μL ethanolamine (Sigma-Aldrich) as a stabilizer. After stirring the solution overnight under ambient conditions, the ZnO solution was spin coated for 30 s at 4,000 rpm onto the ITO substrates and subsequently annealed for 1 h at 200°C to obtain a ZnO layer thickness of roughly 30 nm. PEDOT:PSS solution was first diluted with the same volume of water and then cast at 4,000 rpm on ITO substrates, followed by thermal annealing at 155°C for 15 min to form a 10-nm film. PBDB-T was purchased from Zhiyan (Nanjing, China), and EH-IDTBR was purchased from Solarmer (Beijing, China). A total concentration of 16 mg/mL in CB:DIO (99:1 [v/v]) with a D:A ratio of 1:1 was used to prepare the PBDB-T:EH-IDTBR solution. The solution was spin coated at 900 rpm and thermally annealed at 100°C for 10 min to form a film with a thickness of around 110 nm. PM6 was purchased from Solarmer (Beijing, China), and ITIC was purchased from Zhi-yan (Nanjing, China). A total concentration of 14 mg/mL in CF:DIO (99:1 [v/v]) with a D:A ratio of 1:1 was used to prepare the PM6:ITIC solution. The solution was spin coated at 3,000 rpm and thermally annealed at 100°C for 10 min to form a film with a thickness of around 110 nm. Y6 was purchased from Solarmer (Beijing, China). Here, a total concentration of 16 mg/mL in CF:1-chloronaphthalene (99.5:0.5 [v/v]) with a D:A ratio of 1:1.2 was used to prepare the PM6:Y6 solution. The final solution was spin coated at 3,000 rpm and thermally annealed for 10 min at 100°C to form an active layer film with a thickness of around 100 nm. After spin coating of the PBDB-T:EH-IDTBR, PM6:ITIC, and PM6:Y6 active layer, 7 nm of MoO_3 was evaporated on PBDB-T:EH-IDTBR to form the hole transport layer, while 10 nm of PDINO was spin coated from solution (1.5 mg/mL PDINO at 2,000 rpm) on PM6:ITIC and PM6:Y6 to form the electron transport layer. Finally, 100 nm of Ag was

evaporated as the top electrode on all devices with a pixel area of 0.04 cm^2. The base pressure in the vacuum chamber was less than 10^{-6} mbar. The substrates were then finalized by sealing with a coverglass using UV light-annealed glue from Bluefix. All film thicknesses were measured with a Dektak^{3ST} profilometer.

SUPPLEMENTAL INFORMATION

Supplemental information can be found online at https://doi.org/10.1016/j.xcrp.2022.101096.

ACKNOWLEDGMENTS

This work was supported by the Welsh Government's Sêr Cymru II Program through the European Regional Development Fund, Welsh European Funding Office, and Swansea University strategic initiative in Sustainable Advanced Materials. A.A. is a Sêr Cymru II Rising Star Fellow, and P.M. is a Sêr Cymru II National Research Chair. This work was also funded by UKRI through EPSRC program grant EP/T028511/1, Application Targeted Integrated Photovoltaics.

AUTHOR CONTRIBUTIONS

S.Z. performed the experiments. W.L. fabricated the devices. O.J.S. carried out the theoretical calculations. P.M. and A.A. assisted with analyzing and interpreting the data. O.J.S supervised the work. All authors contributed to development of the manuscript first drafted by S.Z. together with O.J.S.

DECLARATION OF INTERESTS

The authors declare no competing interests.

Received: June 20, 2022
Revised: August 12, 2022
Accepted: September 20, 2022
Published: October 10, 2022

REFERENCES

1. Xu, Y., Yao, H., and Hou, J. (2019). Recent advances in fullerene-free polymer solar cells: materials and devices. Chin. J. Chem. *37*, 207–215. https://doi.org/10.1002/cjoc.201800471.

2. Ren, H., Chen, J.D., Li, Y.Q., and Tang, J.X. (2020). Recent progress in organic photodetectors and their applications. Adv. Sci. *8*, 2002418. https://doi.org/10.1002/advs.202002418.

3. Armin, A., Li, W., Sandberg, O.J., Xiao, Z., Ding, L., Nelson, J., Neher, D., Vandewal, K., Shoaee, S., Wang, T., et al. (2021). A history and perspective of non-fullerene electron acceptors for organic solar cells. Adv. Energy Mater. *11*, 2003570. https://doi.org/10.1002/aenm.202003570.

4. Xie, L., Song, W., Ge, J., Tang, B., Zhang, X., Wu, T., and Ge, Z. (2021). Recent progress of organic photovoltaics for indoor energy harvesting. Nano. Energy *82*, 105770. https://doi.org/10.1016/j.nanoen.2021.105770.

5. Bartesaghi, D., Pérez, I.D.C., Kniepert, J., Roland, S., Turbiez, M., Neher, D., and Koster, L.J.A. (2015). Competition between recombination and extraction of free charges determines the fill factor of organic solar cells. Nat. Commun. *6*, 7083–7110. https://doi.org/10.1038/ncomms8083.

6. Proctor, C.M., Kuik, M., and Nguyen, T.Q. (2013). Charge carrier recombination in organic solar cells. Prog. Polym. Sci. *38*, 1941–1960. https://doi.org/10.1016/j.progpolymsci.2013.08.008.

7. Laquai, F., Andrienko, D., Deibel, C., and Neher, D. (2017). Charge carrier generation, recombination, and extraction in polymer–fullerene bulk heterojunction organic solar cells. Adv. Polym. Sci. *272*, 267–291. https://doi.org/10.1007/978-3-319-28338-8_11.

8. Deibel, C., and Dyakonov, V. (2010). Polymer-fullerene bulk heterojunction solar cells. Rep. Prog. Phys. *73*, 096401–096439. https://doi.org/10.1088/0034-4885/73/9/096401.

9. Clarke, T.M., and Durrant, J.R. (2010). Charge photogeneration in organic solar cells. Chem. Rev. *110*, 6736–6767. https://doi.org/10.1021/cr900271s.

10. Armin, A., Hambsch, M., Kim, I.K., Burn, P.L., Meredith, P., and Namdas, E.B. (2014). Thick junction broadband organic photodiodes. Laser Photon. Rev. *8*, 924–932. https://doi.org/10.1002/lpor.201400081.

11. Neher, D., Kniepert, J., Elimelech, A., and Koster, L.J.A. (2016). A new figure of merit for organic solar cells with transport-limited photocurrents. Sci. Rep. *6*, 24861. https://doi.org/10.1038/srep24861.

12. Mihailetchi, V.D., Wildeman, J., and Blom, P.W.M. (2005). Space-charge limited photocurrent. Phys. Rev. Lett. *94*, 126602. https://doi.org/10.1103/PhysRevLett.94.126602.

13. Deibel, C., and Wagenpfahl, A. (2010). Comment on "Interface state recombination in organic solar cells". Phys. Rev. B *82*, 207301. https://doi.org/10.1103/PhysRevB.82.207301.

14. Koster, L.J.A., Kemerink, M., Wienk, M.M., Maturová, K., and Janssen, R.A.J. (2011). Quantifying bimolecular recombination losses in organic bulk heterojunction solar cells. Adv. Mater. *23*, 1670–1674. https://doi.org/10.1002/adma.201004311.

15. Maurano, A., Shuttle, C.G., Hamilton, R., Ballantyne, A.M., Nelson, J., Zhang, W., Heeney, M., and Durrant, J.R. (2011). Transient

optoelectronic analysis of charge carrier losses in a selenophene/fullerene blend solar cell. J. Phys. Chem. C *115*, 5947–5957. https://doi.org/10.1021/jp109697w.

16. Kirchartz, T., Deledalle, F., Tuladhar, P.S., Durrant, J.R., and Nelson, J. (2013). On the differences between dark and light ideality factor in polymer:fullerene solar cells. J. Phys. Chem. Lett. *4*, 2371–2376. https://doi.org/10.1021/jz4012146.

17. Tvingstedt, K., and Deibel, C. (2016). Temperature dependence of ideality factors in organic solar cells and the relation to radiative efficiency. Adv. Energy Mater. *6*, 1502230. https://doi.org/10.1002/aenm.201502230.

18. Tress, W., Leo, K., and Riede, M. (2013). Dominating recombination mechanisms in organic solar cells based on ZnPc and C60. Appl. Phys. Lett. *102*, 163901. https://doi.org/10.1063/1.4802276.

19. Shuttle, C.G., O'Regan, B., Ballantyne, A.M., Nelson, J., Bradley, D.D.C., De Mello, J., and Durrant, J.R. (2008). Experimental determination of the rate law for charge carrier decay in a polythiophene: fullerene solar cell. Appl. Phys. Lett. *92*, 093311. https://doi.org/10.1063/1.2891871.

20. Sandberg, O.J., Tvingstedt, K., Meredith, P., and Armin, A. (2019). Theoretical perspective on transient photovoltage and charge extraction techniques. J. Phys. Chem. C *123*, 14261–14271. https://doi.org/10.1021/acs.jpcc.9b03133.

21. Kiermasch, D., Baumann, A., Fischer, M., Dyakonov, V., and Tvingstedt, K. (2018). Revisiting lifetimes from transient electrical characterization of thin film solar cells; A capacitive concern evaluated for silicon, organic and perovskite devices. Energy Environ. Sci. *11*, 629–640. https://doi.org/10.1039/c7ee03155f.

22. Azzouzi, M., Calado, P., Telford, A.M., Eisner, F., Hou, X., Kirchartz, T., Barnes, P.R.F., and Nelson, J. (2020). Overcoming the limitations of transient photovoltage measurements for studying recombination in organic solar cells. Sol. RRL *4*, 1900581. https://doi.org/10.1002/solr.201900581.

23. Sandberg, O.J., Sundqvist, A., Nyman, M., and Österbacka, R. (2016). Relating charge transport, contact properties, and recombination to open-circuit voltage in sandwich-type thin-film solar cells. Phys. Rev. Appl. *5*, 044005. https://doi.org/10.1103/PhysRevApplied.5.044005.

24. Stolterfoht, M., Armin, A., Shoaee, S., Kassal, I., Burn, P., and Meredith, P. (2016). Slower carriers limit charge generation in organic semiconductor light-harvesting systems. Nat. Commun. *7*, 11944. https://doi.org/10.1038/ncomms11944.

25. Zeiske, S., Sandberg, O.J., Zarrabi, N., Li, W., Meredith, P., and Armin, A. (2021). Direct observation of trap-assisted recombination in organic photovoltaic devices. Nat. Commun. *12*, 3603. https://doi.org/10.1038/s41467-021-23870-x.

26. Liraz, D., Cheng, P., Yang, Y., and Tessler, N. (2022). Light-induced trap emptying revealed by intensity-dependent quantum efficiency of organic solar cells. J. Appl. Phys. *131*, 135501. https://doi.org/10.1063/5.0084184.

27. Hartnagel, P., and Kirchartz, T. (2020). Understanding the light-intensity dependence of the short-circuit current of organic solar cells. Adv. Theory Simul. *3*, 2000116. https://doi.org/10.1002/adts.202000116.

28. Tzabari, L., and Tessler, N. (2011). Shockley-Read-Hall recombination in P3HT:PCBM solar cells as observed under ultralow light intensities. J. Appl. Phys. *109*, 064501. https://doi.org/10.1063/1.3549820.

29. Sandberg, O.J., Nyman, M., and Österbacka, R. (2014). Effect of contacts in organic bulk heterojunction solar cells. Phys. Rev. Appl. *1*, 024003. https://doi.org/10.1103/PhysRevApplied.1.024003.

30. Würfel, U., Perdigón-Toro, L., Kurpiers, J., Wolff, C.M., Caprioglio, P., Rech, J.J., Zhu, J., Zhan, X., You, W., Shoaee, S., et al. (2019). Recombination between photogenerated and electrode-induced charges dominates the fill factor losses in optimized organic solar cells. J. Phys. Chem. Lett. *10*, 3473–3480. https://doi.org/10.1021/acs.jpclett.9b01175.

31. Würfel, U., and Unmüssig, M. (2018). Apparent field-dependence of the charge carrier generation in organic solar cells as a result of (bimolecular) recombination. Sol. RRL *2*, 1800229. https://doi.org/10.1002/solr.201800229.

32. Sokel, R., and Hughes, R.C. (1982). Numerical analysis of transient photoconductivity in insulators. J. Appl. Phys. *53*, 7414–7424. https://doi.org/10.1063/1.330111.

33. Wagenpfahl, A., Deibel, C., and Dyakonov, V. (2010). Organic solar cell efficiencies under the aspect of reduced surface recombination velocities. IEEE J. Sel. Top. Quantum Electron. *16*, 1759–1763. https://doi.org/10.1109/JSTQE.2010.2042142.

34. Wehenkel, D.J., Koster, L.J.A., Wienk, M.M., and Janssen, R.A.J. (2012). Influence of injected charge carriers on photocurrents in polymer solar cells. Phys. Rev. B *85*, 125203. https://doi.org/10.1103/PhysRevB.85.125203.

35. Kaienburg, P., Rau, U., and Kirchartz, T. (2016). Extracting information about the electronic quality of organic solar-cell absorbers from fill factor and thickness. Phys. Rev. Appl. *6*, 024001–024015. https://doi.org/10.1103/PhysRevApplied.6.024001.

36. Phuong, L.Q., Hosseini, S.M., Sandberg, O.J., Zou, Y., Woo, H.Y., Neher, D., and Shoaee, S. (2021). Quantifying quasi-fermi level splitting and open-circuit voltage losses in highly efficient nonfullerene organic solar cells. Sol. RRL *5*, 2000649. https://doi.org/10.1002/solr.202000649.

37. Armin, A., Subbiah, J., Stolterfoht, M., Shoaee, S., Xiao, Z., Lu, S., Jones, D.J., and Meredith, P. (2016). Reduced recombination in high efficiency molecular nematic liquid crystalline: fullerene solar cells. Adv. Energy Mater. *6*, 1600939. https://doi.org/10.1002/aenm.201600939.

38. Stolterfoht, M., Armin, A., Philippa, B., and Neher, D. (2016). The role of space charge effects on the competition between recombination and extraction in solar cells with low-mobility photoactive layers. J. Phys. Chem. Lett. *7*, 4716–4721. https://doi.org/10.1021/acs.jpclett.6b02106.

39. Wilken, S., Sandberg, O.J., Scheunemann, D., and Österbacka, R. (2019). Watching space charge build up in an organic solar cell. Sol. RRL *4*, 1900505. https://doi.org/10.1002/solr.201900505.

40. Kirchartz, T., Agostinelli, T., Campoy-Quiles, M., Gong, W., and Nelson, J. (2012). Understanding the thickness-dependent performance of organic bulk heterojunction solar cells: the influence of mobility, lifetime, and space charge. J. Phys. Chem. Lett. *3*, 3470–3475. https://doi.org/10.1021/jz301639y.

41. Ooi, Z.E., Chan, K.L., Lombardo, C.J., and Dodabalapur, A. (2012). Analysis of photocurrents in lateral-geometry organic bulk heterojunction devices. Appl. Phys. Lett. *101*, 053301. https://doi.org/10.1063/1.4739469.

42. Deledalle, F., Kirchartz, T., Vezie, M.S., Campoy-Quiles, M., Shakya Tuladhar, P., Nelson, J., and Durrant, J.R. (2015). Understanding the effect of unintentional doping on transport optimization and analysis in efficient organic bulk-heterojunction solar cells. Phys. Rev. X *5*, 011032. https://doi.org/10.1103/PhysRevX.5.011032.

43. Sandberg, O.J., Dahlström, S., Nyman, M., Wilken, S., Scheunemann, D., and Österbacka, R. (2019). Impact of a doping-induced space-charge region on the collection of photogenerated charge carriers in thin-film solar cells based on low-mobility semiconductors. Phys. Rev. Appl. *12*, 034008. https://doi.org/10.1103/PhysRevApplied.12.034008.

44. Kirchartz, T., Gong, W., Hawks, S.A., Agostinelli, T., MacKenzie, R.C.I., Yang, Y., and Nelson, J. (2012). Sensitivity of the mott-Schottky analysis in organic solar cells. J. Phys. Chem. C *116*, 7672–7680. https://doi.org/10.1021/jp300397f.

45. Goodman, A.M., and Rose, A. (1971). Double extraction of uniformly generated electron-hole pairs from insulators with noninjecting contacts. J. Appl. Phys. *42*, 2823–2830. https://doi.org/10.1063/1.1660633.

46. Crandall, R.S. (1982). Transport in hydrogenated amorphous silicon p-i-n solar cells. J. Appl. Phys. *53*, 3350–3352. https://doi.org/10.1063/1.331002.

47. Gudden, B., and Pohl, R. (1924). Zum Mechanismus des lichtelektrischen Primärstromes in Kristallen. Z. Physik *30*, 14–23. https://doi.org/10.1007/BF01331819.

48. Hüpkes, J., Rau, U., and Kirchartz, T. (2022). Dielectric junction: electrostatic design for charge carrier collection in solar cells. Sol. RRL *6*, 2100720. https://doi.org/10.1002/solr.202100720.

49. Kirchartz, T., Pieters, B.E., Kirkpatrick, J., Rau, U., and Nelson, J. (2011). Recombination via tail states in polythiophene:fullerene solar cells. Phys. Rev. B *83*, 115209. https://doi.org/10.1103/PhysRevB.83.115209.

50. Street, R.A. (2011). Localized state distribution and its effect on recombination in organic solar cells. Phys. Rev. B *84*, 075208. https://doi.org/10.1103/PhysRevB.84.075208.

51. Beuel, S., Hartnagel, P., and Kirchartz, T. (2021). The influence of Photo-induced space charge and Energetic Disorder on the indoor and outdoor performance of organic solar cells. Adv. Theory Simul. *4*, 2000319. https://doi.org/10.1002/adts.202000319.

52. Wu, J., Luke, J., Lee, H.K.H., Shakya Tuladhar, P., Cha, H., Jang, S.Y., Tsoi, W.C., Heeney, M., Kang, H., Lee, K., et al. (2019). Tail state limited photocurrent collection of thick photoactive layers in organic solar cells. Nat. Commun. *10*, 5159. https://doi.org/10.1038/s41467-019-12951-7.

53. Pettersson, L.A.A., Roman, L.S., and Inganäs, O. (1999). Modeling photocurrent action spectra of photovoltaic devices based on organic thin films. J. Appl. Phys. *86*, 487–496. https://doi.org/10.1063/1.370757.

54. Armin, A., Zarrabi, N., Sandberg, O.J., Kaiser, C., Zeiske, S., Li, W., and Meredith, P. (2020). Limitations of charge transfer state parameterization using ohotovoltaic external quantum efficiency. Adv. Energy Mater. *10*, 2001828. https://doi.org/10.1002/aenm.202001828.

55. Nyman, M., Sandberg, O.J., Li, W., Zeiske, S., Kerremans, R., Meredith, P., and Armin, A. (2021). Requirements for making thick junctions of organic solar cells based on nonfullerene acceptors. Sol. RRL *5*, 2100018. https://doi.org/10.1002/solr.202100018.

56. Ullbrich, S., Fischer, A., Tang, Z., Ávila, J., Bolink, H.J., Reineke, S., and Vandewal, K. (2018). Electrothermal feedback and absorption-induced open-circuit-voltage turnover in solar cells. Phys. Rev. Appl. *9*, 051003. https://doi.org/10.1103/PhysRevApplied.9.051003.

57. Riley, D.B., Sandberg, O.J., Li, W., Meredith, P., and Armin, A. (2022). Quasi-steady-state measurement of exciton diffusion lengths in organic semiconductors. Phys. Rev. Appl. *17*, 024076. https://doi.org/10.1103/PhysRevApplied.17.024076.

58. Li, W., Zeiske, S., Sandberg, O.J., Riley, D.B., Meredith, P., and Armin, A. (2021). Organic solar cells with near-unity charge rgeneration yield. Energy Environ. Sci. *14*, 6484–6493. https://doi.org/10.1039/d1ee01367j.

59. Yazmaciyan, A., Stolterfoht, M., Burn, P.L., Lin, Q., Meredith, P., and Armin, A. (2018). Recombination losses above and below the transport percolation threshold in bulk heterojunction organic solar cells. Adv. Energy Mater. *8*, 1703339. https://doi.org/10.1002/aenm.201703339.

60. Tromholt, T., Madsen, M.V., and Krebs, F.C. (2013). Ultra high opren circuit voltage (>1 V) of poly-3-hexylthiophene based organic solar cells with concentrated light. Appl. Phys. Lett. *102*, 123904. https://doi.org/10.1063/1.4798585.